

This is the accepted manuscript made available via CHORUS. The article has been published as:

Thermoelastic properties of α -iron from first-principles

Daniele Dragoni, Davide Ceresoli, and Nicola Marzari

Phys. Rev. B **91**, 104105 — Published 5 March 2015

DOI: [10.1103/PhysRevB.91.104105](https://doi.org/10.1103/PhysRevB.91.104105)

Thermoelastic properties of α -iron from first-principles

Daniele Dragoni,¹ Davide Ceresoli,² and Nicola Marzari¹

¹*Theory and Simulations of Materials (THEOS),
and National Center for Computational Design
and Discovery of Novel Materials (MARVEL),*

École Polytechnique Fédérale de Lausanne, 1015 Lausanne, Switzerland

²*CNR Istituto di Scienze e Tecnologie Molecolari (CNR-ISTM), 20133, Milano, Italy*

(Dated: January 23, 2015)

Abstract

We calculate the thermomechanical properties of α -iron, and in particular its isothermal and adiabatic elastic constants, using first-principles total-energy and lattice-dynamics calculations, minimizing the quasi-harmonic vibrational free energy under finite strain deformations. Particular care is made in the fitting procedure for the static and temperature-dependent contributions to the free energy, in discussing error propagation for the two contributions separately, and in the verification and validation of pseudopotential and all-electron calculations. We find that the zero-temperature mechanical properties are sensitive to the details of the calculation strategy employed, and common semi-local exchange-correlation functionals provide only fair to good agreement with experimental elastic constants, while their temperature dependence is in excellent agreement with experiments in a wide range of temperature almost up to the Curie transition.

I. INTRODUCTION

Elemental iron is a material of great scientific and economic interest: it's the major constituent of steels, it determines the properties of the earth core, and its complex phase diagram is driven by the subtle interplay between vibrational and magnetic contributions, making it particularly challenging to describe accurately from first-principles. This is especially relevant as temperature increases, since magnetic excitations become important and a dramatic change in the magnetic nature of the system takes place. At ordinary pressures, iron turns from a BCC ferromagnet to a BCC paramagnet with a second-order transition ($\alpha \rightarrow \beta$) at a Curie temperature of ~ 1043 K. This transition is then followed by two structural transitions, a BCC \rightarrow FCC ($\beta \rightarrow \gamma$) transition at 1185 K and a FCC \rightarrow BCC ($\gamma \rightarrow \delta$) transition at 1670 K, before finally melting at ~ 1814 K.

First-principles simulations can be a key technique and a valid alternative to experiments in order to get accurate predictions of phase diagrams without the need of phenomenological parameters, and become essential at conditions that are challenging to reproduce in real life, like those inside the earth's core¹. For the case of pressure-temperature phase diagrams, zero-temperature first-principles equations of state can be supplemented with finite-temperature vibrational entropies, that can be derived directly from the knowledge of the phonon dispersions. These latter can be calculated from finite differences, or more elegantly and less expensively with density-functional perturbation theory (DFPT)^{2,3}. When coupled to the quasi-harmonic approximation⁴ (QHA), these techniques allow to calculate thermal expansion and vibrational properties at finite temperatures, often well above the Debye temperature^{5–11}. While there have been numerous first-principles calculations of elastic properties of solids by either total energy, stress-strain^{12,13} or density-functional perturbation theory approaches^{14–16} a relatively limited number of them has been focused on to the thermo-mechanical properties of metals or minerals^{17–20}.

In this paper, we calculate the adiabatic and isothermal finite-temperature elastic properties of ferromagnetic α -iron at ambient pressure and in the temperature range of stability for ferromagnetic α -iron using the QHA and DFPT. We also carefully explore multidimensional fitting procedures for the static and vibrational contributions to the free energy, and analyze the quality of the fit and the source of errors of both contributions, providing a confidence interval of each elastic constant as a function of temperature.

The paper is organized as follows: in Sec. II we introduce the finite strain framework used to calculate the elastic constants, and in Sec. III we give the computational details of our first-principles density-functional theory (DFT) and DFTP calculations. We present our results and their comparison to experiments in Sec. IV. Finally, Section V is devoted to summary and conclusions.

II. FINITE-STRAIN METHOD

In the limit of small deformations, the energy of a crystal at an arbitrary configuration can be Taylor-expanded in terms of a symmetric matrix $\boldsymbol{\varepsilon}$ describing a uniform linear deformation \mathbf{A} such that

$$\mathbf{A} = \mathbf{1} + \boldsymbol{\varepsilon} \quad (1)$$

and any position vector \bar{r} in the reference configuration is transformed into $(\mathbf{1} + \boldsymbol{\varepsilon}) \cdot \bar{r}$. The isothermal elastic constants (SOECs) at zero pressure are then defined as the second-order coefficients of this expansion according to²¹

$$C_{ij}^T = \frac{1}{V_0} \left. \frac{\partial^2 F}{\partial \varepsilon_i \partial \varepsilon_j} \right|_{V_0, T}, \quad (2)$$

where F is the Helmholtz free-energy and $\varepsilon_i, \varepsilon_j, i, j = 1 \dots 6$ are the components of the strain tensor $\boldsymbol{\varepsilon}$ (we adopt here the Voigt notation). Also, note that the second derivatives are evaluated at the thermodynamic equilibrium configuration with volume V_0 and at constant temperature T .

For cubic crystals, like α -iron, only three elastic constants are needed to completely determine the stiffness tensor and, therefore, fully characterize the mechanical response of the system in the linear elastic regime. As a consequence only three independent deformations are sufficient, and we choose here the hydrostatic, tetragonal and trigonal deformations, shown in Tab. I. Each deformation fully determines one of the cubic elastic constants (or elastic moduli).

In order to compute finite-temperature properties and, therefore, to calculate the Helmholtz free energy F , the vibrational contributions must be added to the static energy contributions. The QHA⁴ provides an analytical expression for the vibrational contribution

$\boldsymbol{\varepsilon}^{(i)}$	ε_1	ε_2	ε_3	ε_4	ε_5	ε_6
$\boldsymbol{\varepsilon}^{(1)}$	ε_a	ε_a	ε_a	0	0	0
$\boldsymbol{\varepsilon}^{(2)}$	0	0	ε_c	0	0	0
$\boldsymbol{\varepsilon}^{(3)*}$	0	0	0	$\varepsilon_d/2$	$\varepsilon_d/2$	$\varepsilon_d/2$

TABLE I. Deformations and corresponding strain vectors in the Voigt notation: ⁽¹⁾hydrostatic, ⁽²⁾tetragonal and ⁽³⁾trigonal deformations are governed by a single parameter. *Note that the trigonal deformation reported here is the first-order expansion of the full strain tensor $\boldsymbol{\varepsilon}^{(3)}$ with non-zero off-diagonal terms.

to the free energy:

$$\begin{aligned}
F(\{a_i\}, T) = & \underbrace{E_{stat}(\{a_i\})}_{\text{Static}} + \underbrace{\frac{1}{2} \sum_{\mathbf{q}, \lambda} \hbar \omega_{\mathbf{q}, \lambda}(\{a_i\})}_{\text{ZPE}} + \\
& \underbrace{k_B T \sum_{\mathbf{q}, \lambda} \ln \left(1 - e^{-\frac{\hbar \omega_{\mathbf{q}, \lambda}(\{a_i\})}{k_B T}} \right)}_{\text{Thermal}}, \tag{3}
\end{aligned}$$

where the sum is performed over all the phonon modes λ and all the phonon wave vectors \mathbf{q} spanning the Brillouin zone (BZ). Here, k_B is the Boltzmann constant and $\omega_{\mathbf{q}, \lambda}$ the vibrational frequencies of the different phonon modes, where in the QHA their explicit dependence on the geometry of the system via the primitive lattice vectors $\{a_i\}$ is accounted for. The vibrational part, coming directly from the analytic partition function of a Bose-Einstein gas of harmonic oscillators, can be split into a zero-point energy term plus a contribution which depends explicitly on the temperature T . We neglect here the thermal electronic effects, because they are believed to be small compared to the quasi-harmonic vibrational contribution^{11,22} in the range of stability of the α phase. Magnetic effects are also not considered, except for the longitudinal relaxation of the total magnetic moment as a function of strain, but they are known to be important approaching the Curie point^{23–25} and their influence on the elastic properties is briefly discussed in Sec. IV C in the light of previous studies.

Eq. 2 is used to calculate the isothermal elastic constants at finite temperature; however, in order to compare results with experimental data obtained from ultrasonic measurements²⁶,

we also calculate the adiabatic elastic constants, using the following relations²¹

$$\begin{aligned}
C_{11}^{(S)} - C_{11}^{(T)} &= C_{12}^{(S)} - C_{12}^{(T)} = \\
&= B^{(S)} - B^{(T)} = \frac{T V \alpha^2 B^{(T)^2}}{C_V}, \\
C_{44}^{(S)} - C_{44}^{(T)} &= 0,
\end{aligned} \tag{4}$$

where the heat capacity at constant volume C_V and the volumetric thermal expansion coefficient α are both calculated from the QHA. The superscripts (S) and (T) define the adiabatic and isothermal elastic constants C_{ij} and bulk modulus B respectively.

III. COMPUTATIONAL DETAILS AND PSEUDOPOTENTIAL SELECTION

We calculate the first-principles elastic constants using DFT, as implemented in the **PWSCF** and **PHONON** packages of the **QUANTUM-ESPRESSO** distribution²⁷ for the static and lattice dynamical calculations, respectively. The calculations are spin-polarized and the magnetic moment is free to vary collinearly in order to minimize the total energy. In all calculations the exchange-correlation effects have been treated within the generalized-gradient approximation (GGA) with the PBE functional²⁸. We use an ultrasoft pseudopotential²⁹ (USPP) from *pslibrary.0.3.0*³⁰, which includes also $3s$ and $3p$ semicore states³¹ (i.e. 16 valence electrons) along with a plane-wave basis with a wavefunction kinetic-energy cutoff of 90 Ry and a cutoff of 1080 Ry for the charge density. We sampled the BZ with an offset $24 \times 24 \times 24$ Monkhorst-Pack k -mesh, with a Marzari-Vanderbilt smearing³² of 0.005 Ry.

Phonon calculations were carried out for each deformation within DFPT³: the dynamical matrix and its eigenvalues are calculated on a $4 \times 4 \times 4$ mesh of special points in the BZ and Fourier-interpolated on an extended $21 \times 21 \times 21$ grid for the integration of thermodynamic quantities. We arrived at this computational setup (cutoff, smearing and BZ sampling) after a careful investigation of the convergence of total energy and individual phonon frequencies for different deformations. Also, we verified that individual total energies and phonon frequencies do change smoothly as a function of strain.

Since the choice of the pseudopotential is of primary importance for a clear comparison with computational and experimental data in the literature, it is worth to stress that the one used here has been chosen among different candidates from the *pslibrary*³³ and *GBRV*

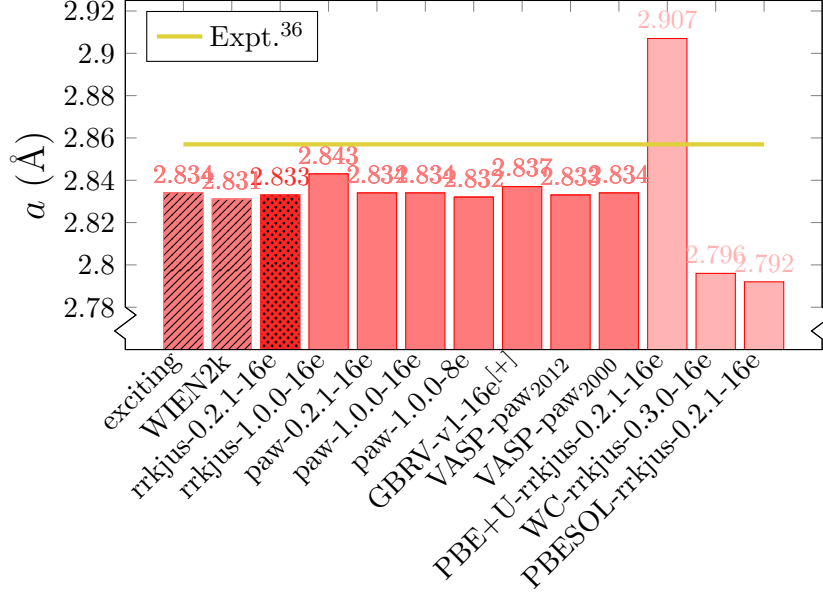


FIG. 1. Equilibrium lattice parameter at 0 K for the different iron pseudopotentials tested in this work. All the data shown here are obtained with the PBE XC functional except for the last three columns on the right, where we have used PBE+U^{37–40}, WC⁴¹ and a PBEsol⁴² respectively (here we use a Hubbard U correction with $U = 3\text{eV}$). The data come from a Birch-Murnaghan fit, do not include zero-point energy and are compared to all-electron WIEN2K⁴³, **exciting**⁴⁴ and VASP³⁵ calculations from Ref. 45–47 respectively and experiments^{36,48,49} (horizontal yellow line). The crosshatch dotted column corresponds to the pseudopotential chosen for the production runs.

library³⁴ to reproduce, as closely as possible, the all-electron FLAPW equilibrium lattice parameter, bulk modulus at 0 K and local magnetization obtained from independent groups. Also, for the sake of completeness, we compare against results obtained using the VASP code and associated pseudopotentials³⁵.

These values in Figs. 1, 2 are obtained from a Birch-Murnaghan fit of calculated $E(V)$ data points. Interestingly, we have found that the volume range of validity for fitting a Birch-Murnaghan curve is limited on the expansion side due to anomalies in the $E(V)$ curve and its derivatives. These anomalies, also reported for all-electron and other calculation methods in Ref. 52, are more clearly visible as “shoulders” in the $M(V)$ behavior (see Fig. 3) and, as visible from Fig. 4, can be associated to a smooth magnetic transition from a low to high spin state due to the splitting of the majority and minority spin t_{2g} electrons upon increasing the volume. However, for the pseudopotential chosen here, the expanded volumes at which

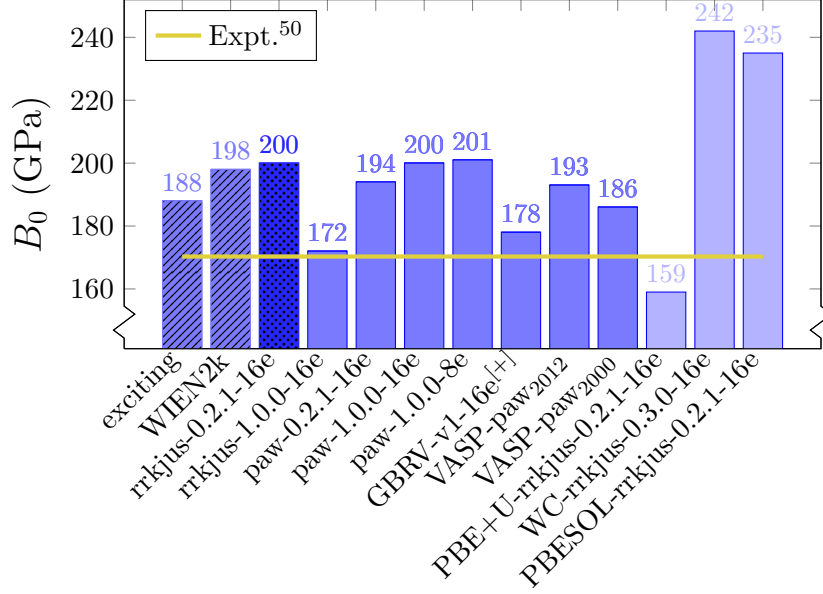


FIG. 2. Equilibrium bulk moduli at 0 K for the different iron pseudopotentials tested in this work. All the data shown here are obtained with the PBE XC functional except for the last three columns on the right, where we have used PBE+U^{37–40}, WC⁴¹ and a PBEsol⁴² respectively (we use here a Hubbard U correction with $U = 3eV$). The data come from a Birch-Murnaghan fit, do not include zero-point energy and are compared to all-electron WIEN2K⁴³, **exciting**⁴⁴ and VASP³⁵ calculations from Ref. 45–47 respectively and experiments⁵⁰ (horizontal yellow line). The crosshatch dotted column corresponds to the pseudopotential chosen for the production runs.

this anomaly is observed (above 9%⁵³) are far beyond the theoretical thermal expansion of the system in the thermodynamic region considered in this work, thus enabling us to fit the energy surface with volume expansions up to $\sim 9\%$ still using a standard Birch-Murnaghan equation.

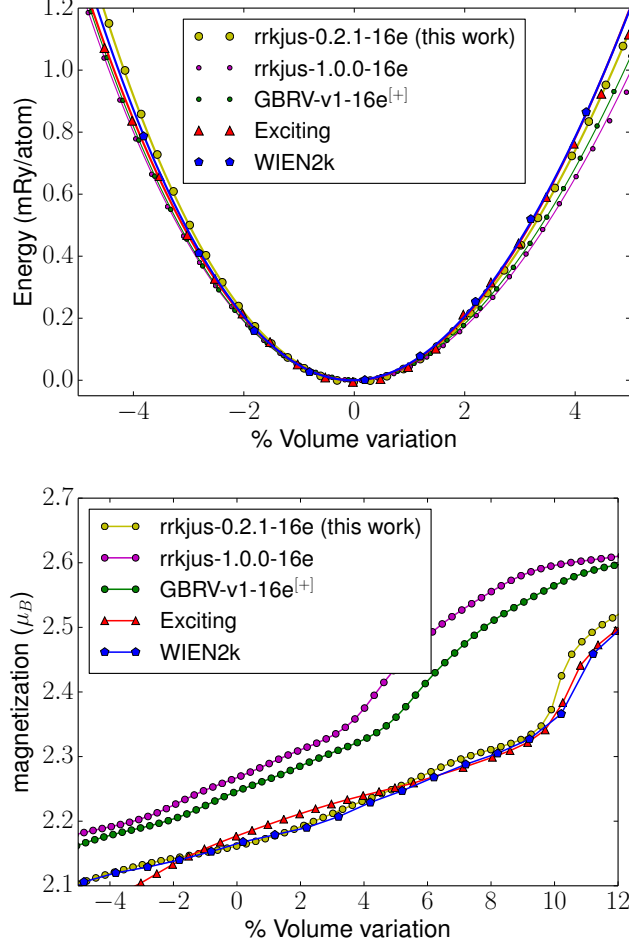


FIG. 3. (Top panel) Equation of state as a function of percent volume change with respect to the theoretical equilibrium configurations for three of the selected PBE pseudopotentials considered in this work (circles). The yellow circles best match the all-electron WIEN2K⁴³ (pentagons) and **exciting**⁴⁴ (triangles) results from Ref. 46 and 51 and correspond to the **rrkjus-0.2.1-16e** pseudopotential used in this work. Continuous lines are the best fit of the Birch-Murnaghan equation. (Bottom panel) Total magnetization as a function of percent volume change. The soft magnetic transition discussed in the text is visible as a clear change in the average slope of the different curves.

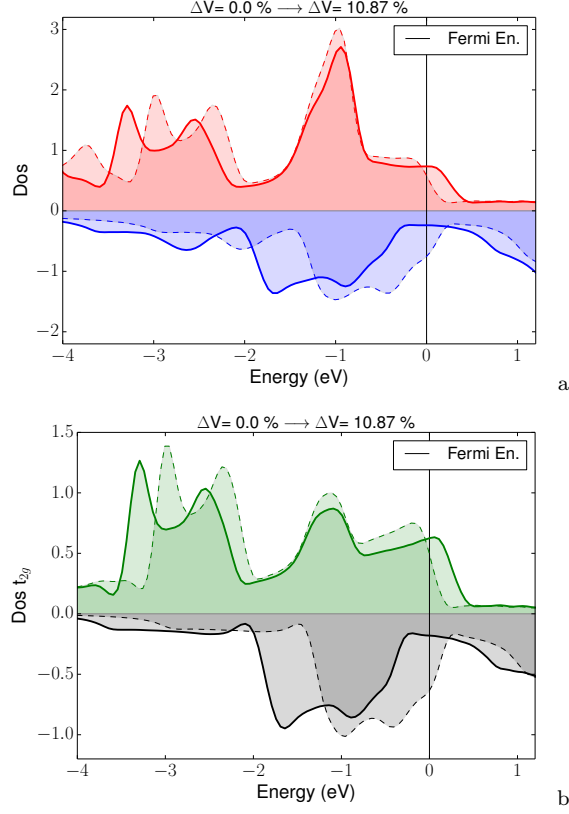


FIG. 4. [a] DOS of majority/minority (red/blue) spin channels at the equilibrium (solid line) and $\Delta V \approx 11\%$ (dashed line) where, for the pseudopotential used in production run, the magnetic transition takes place. [b] The contribution of the t_{2g} electrons to the majority/minority DOS (green/black) is also reported. To obtain a smooth DOS, a non-self-consistent calculation with an offset $60 \times 60 \times 60$ Monkhorst-Pack k -mesh is performed on top of a scf loop.

IV. RESULTS

In this section we present results for selected thermodynamic quantities and for the three strain deformations (hydrostatic or volumetric, tetragonal, and trigonal). Each deformation determines uniquely one of the three elastic constants: B (bulk modulus), C_{11} and C_{44} respectively.

A. B – Volumetric strain

The volumetric deformation $\epsilon^{(1)}$ can be described by a single parameter ϵ_a , namely, the strain of the cubic lattice parameter (see Tab. I). Thus, the lattice spacing is defined as:

$$a = a_0(1 + \epsilon_a) \quad (5)$$

where a_0 is the theoretical equilibrium lattice parameter without zero-point contribution (see Tab. III). The static part of the Helmholtz free energy of Sec. II is obtained by fitting a Birch-Murnaghan equation of state⁵⁴ to a series of well converged total energy values calculated on a one dimensional regular grid with ϵ_a going from -0.02 to $+0.03$ in steps of 0.001 . The resulting static contribution to the bulk modulus is reported in Tab. III. The vibrational contribution, on the other hand, has been calculated on a coarser grid via integration of the phonon dispersions as from Eq. 3 (examples for the calculated phonon dispersion and resulting Grüneisen parameters can be found in Fig. 5), with ϵ_a ranging from -0.012 to $+0.020$ in increments of 0.004 and fitted with a second-order polynomial as a function of the strain parameter ϵ_a . The stability of the results has been checked against a fit with lower and higher order polynomials (see Supplemental Material⁵⁵).

The free energy is then obtained as an analytical function of ϵ_a and T and is shown in Fig. 6. We then determined the thermal expansion (Fig. 6), the thermal expansion coefficients (Fig. 7), the heat capacity (Fig. 7) and the isothermal bulk modulus $B^{(T)}(T)$ from the analytic second derivative of the free energy as in Eq. 1. The adiabatic correction of Eq. 4 is then used to compute the adiabatic bulk modulus $B^{(S)}(T)$. Results are reported in Fig. 8 and compared to experimental data from Refs. 26 and 50. The agreement between experiments and calculations in the thermal behavior of the bulk modulus is remarkable, especially below the Debye temperature ($\Theta_D \simeq 500$ K). Above Θ_D , the small deviation from experiments can be ascribed to magnetic fluctuations^{25,26,63,64} that become increasingly important

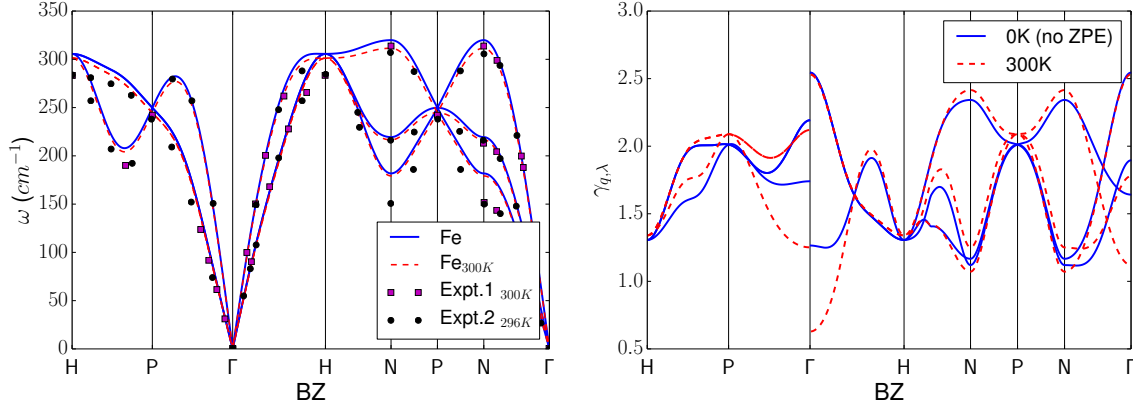


FIG. 5. (Left panel) Phonon dispersions along high-symmetry directions in the BZ calculated at the theoretical electronic equilibrium volume (blue solid line) and at the quasi-harmonic theoretical equilibrium volume at 300 K (red dashed line). The results (see also Fig. 1 in Supplemental Material ^a and Ref. 8 or Ref. 56 for comparison with previous theoretical data) are compared to experimental data at room temperature from Ref. 57 (Expt.1 – squares) and Ref. 58 (Expt.2 – circles). (Right panel) Grüneisen parameters calculated along the same path in the BZ and the same equilibrium volumes used for the phonon dispersion (blue solid line for the 0 K case and red dashed line for the 300 K case). The Grüneisen parameters are obtained computing the first derivative with respect to the volume of a cubic fit of the phonon frequencies.

^a See EPAPS Document No.[]

approaching the Curie temperature (1043 K), plus minor contributions from anharmonic effects (beyond quasi-harmonic) and from the electronic entropy. At 1000 K, the softening of the calculated $B^{(S)}$ is nearly 15% with respect 0 K. The calculated magnetic moment increases from $2.17 \mu_B$ per atom ($2.22 \mu_B$ from experiments⁶⁵) at the 0 K equilibrium volume to $2.27 \mu_B$ at the 1000 K equilibrium volume. Obviously, transverse magnetic fluctuations are neglected in these calculations, and we postpone to Sec. IVC the discussion on the mismatch between experiments and calculations in absolute values.

B. C_{11} , C_{44} – Tetragonal and Trigonal strains

The Helmholtz free energy F depends upon two strain parameters: the isotropic lattice strain ε_a and a second strain parameter ε_c or ε_d according to the deformation considered

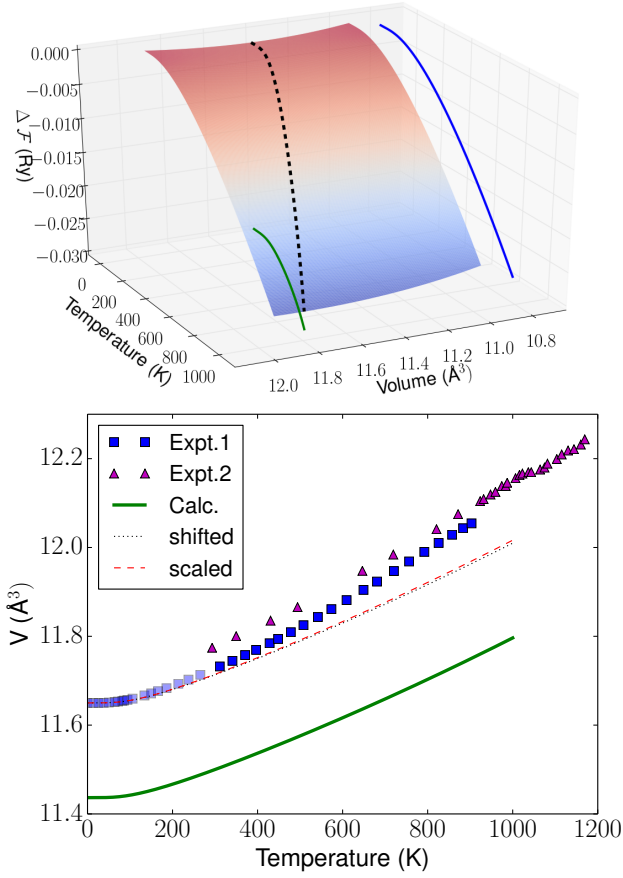


FIG. 6. (Top panel) Free-energy landscape of cubic BCC iron as a function of volume V and temperature T . The dashed black line corresponds to the set of points that minimize the free-energy surface at each temperature. The continuous green and blue lines are the projections of the black dashed line in the T - V and F - T planes, thus describing the volumetric thermal expansion and the zero-pressure free energy as a function of T . (Bottom panel) Volumetric thermal expansion (green solid line) compared to experimental data from Ref. 36 (Expt.1 – blue squares, note that below room temperature the data are extrapolated according to the thermal expansion coefficient of Ref. 49) and Ref. 59 (Expt.2 – magenta triangles). As a guide to the eye, we also report in all plots shifted and scaled quantities. The former are rigidly translated on the vertical axis while the latter are multiplied by a constant factor to match the experimental 0 K value.

(see Tab. I).

The tensor $\epsilon^{(2)}$ is associated to a continuous tetragonal deformation that stretches the edge c of the cubic undistorted structure along the z axis while leaving unchanged the other

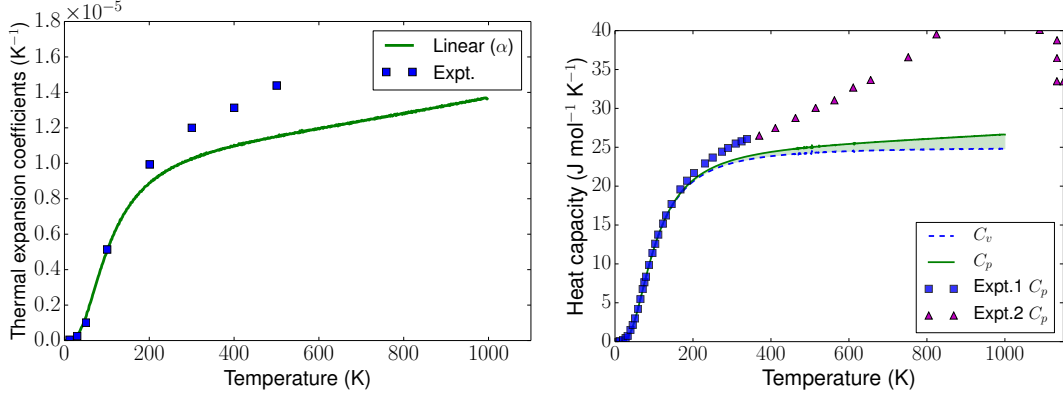


FIG. 7. (Left panel) Linear (green solid line) coefficient of thermal expansion compared to experimental data from Ref. 60 (squares). (Right panel) Specific heat at constant pressure (green solid line), at constant volume (blue dashed line), and compared to experimental data from Ref. 61 (Expt.1 – squares) and from Ref. 62 (Expt.2 – triangles) .

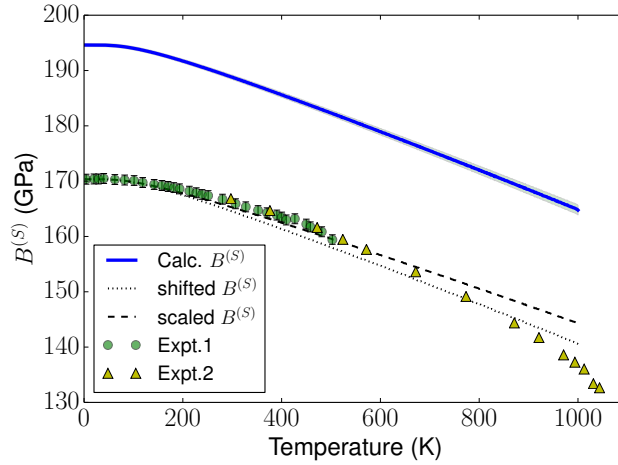


FIG. 8. Adiabatic bulk modulus as a function of T (blue continuous line) calculated along with its confidence interval on the fit (shaded green) and compared to experimental data from Ref. 50 (Expt.1 – green circles) and from Ref. 26 (Expt.2 – yellow triangles). As a guide to the eye, we also plot the bulk modulus rigidly shifted (dotted line) and scaled (dashed line) to match the experimental 0 K value.

edges. The relation between the strain ε_c and the distorted edge c is:

$$c = a(1 + \varepsilon_c). \quad (6)$$

The tensor $\varepsilon^{(3)}$ is associated to a continuous trigonal deformation that stretches the main

diagonal d of the undistorted cubic structure along the (111) direction while tilting the undistorted edges and preserving their length. In this case, the relation between the strain ε_d and the distorted main diagonal is

$$d = \sqrt{3}a(1 + \varepsilon_d), \quad (7)$$

while the relation with the cosine of the angle between the distorted edges is

$$\cos(\alpha) = \frac{1 - \varepsilon_d(2 + \varepsilon_d)}{(\varepsilon_d - 1)(\varepsilon_d + 3)}. \quad (8)$$

Both deformations do not conserve the volume per atom. In particular, in the tetragonal one the volume increases as a function of ε_c , while in the trigonal case, the volume decreases as a function of ε_d . Alternatively, we could have chosen volume-conserving deformations as in Ref. 17, but the advantage of the present scheme is that each deformation determines uniquely one elastic constant at the time, and enables us to determine easily the confidence interval of each elastic constant by error-propagation theory.

In the next sub-sections we describe the calculation of the static and vibrational contributions, separately. The reason is that we want to analyze their contributions to the global energy landscape separately. This also allows us to sample the two contribution landscapes with two different grids. Indeed, the static term displays a minimum as a function of the strain parameters and has to be sampled with a dense grid, while, on the other hand, the vibrational term is flat, monotonic and can be sampled with a coarse grid.

1. *Static contribution*

To evaluate the static contribution to the elastic constants, we performed a series of well converged total energy calculations on a two dimensional discrete grid $[\varepsilon_a, \varepsilon_{c/d}]$ (see Fig. 9 for details on the grid). The ε_a grid is asymmetric with respect to zero and with more points in the positive range of the strain parameter, in order to sample accurately the values of the static contribution to the free energy also in the thermal expansion range.

The resulting total energies are fitted with a two-dimensional bivariate polynomial up to 5th degree using a least-square method⁶⁶.

The analysis of the quality of the fit of discrete data points to a two-dimensional energy surface is crucial to resolve the possible sources of error that could affect our elastic constants

Order	AAE (Ry)	R^2	AAE (Ry)	R^2
	tetragonal		trigonal	
2	1.894 10^{-5}	0.997259	9.163 10^{-5}	0.971580
3	1.997 10^{-6}	0.999975	7.369 10^{-6}	0.999819
4	1.002 10^{-6}	0.999993	2.933 10^{-6}	0.999968
5	9.150 10^{-7}	0.999995	1.693 10^{-6}	0.999990

TABLE II. Average absolute error (AAE) and adjusted coefficient of determination (R^2) of the two-dimensional fit of the static energy landscape, for the tetragonal and trigonal deformations, as a function of the order of the polynomial.

and, therefore, for a reliable comparison with experiments and the wide range of scattered data available in the literature. Therefore, in addition to the visual inspection of the fit along constant $\varepsilon_{c/d}$ sections, we evaluated the adjusted coefficient of determination (R^2) and the the average absolute error (AAE), defined as:

$$\text{AAE} \equiv \frac{1}{N} \sum_{i,j} \left| P_n(\varepsilon_a^{(i)}, \varepsilon_{c/d}^{(j)}) - E(\varepsilon_a^{(i)}, \varepsilon_{c/d}^{(j)}) \right|, \quad (9)$$

where N is the total number of $[\varepsilon_a, \varepsilon_{c/d}]$ discrete values and P_n is the bivariate polynomial of degree n . Thus, R^2 is a measure of the quality of the fitting model, i.e. how well the analytic function approximates the calculated data points. The AAE is a quantitative measure of the distance of the fitted curve from the calculated points. We found that the AAE decreases by increasing the degree n of the polynomial and R^2 approaches unity, as shown in Tab. II. According to these results, in both cases, we considered the 4th-degree polynomial to provide a sufficiently accurate fit (indeed the AAE is two orders of magnitude smaller than the difference between the highest and the lowest total-energy data points).

Fig. 9 shows a plot of the static energy landscape for both the tetragonal and trigonal deformations, with the minimum elongated along the diagonal in the $[\varepsilon_a, \varepsilon_c]$ space or along constant ε_d in the $[\varepsilon_a, \varepsilon_d]$ space.

2. Vibrational contribution

In order to evaluate the vibrational contributions to the free energy, we performed a series of linear-response phonon calculations on a two dimensional grid in the space of deformation

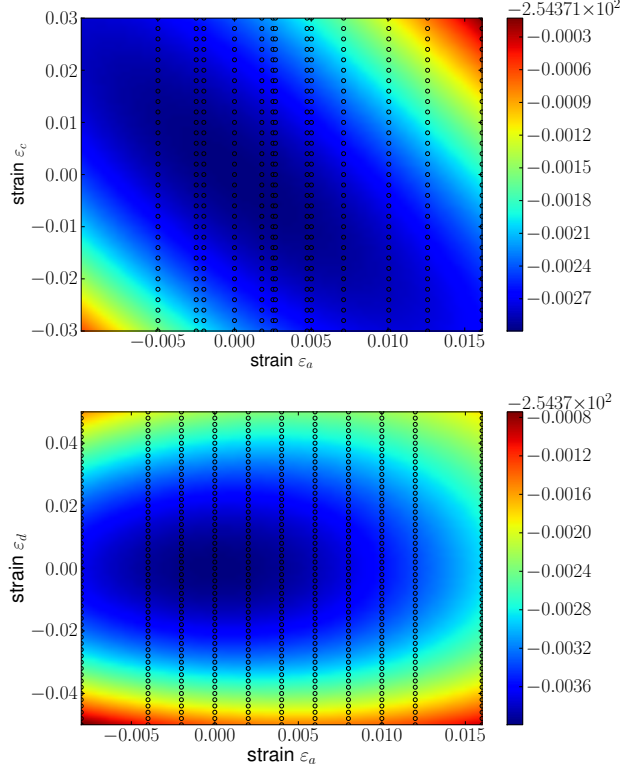


FIG. 9. Static energy landscape of the tetragonal (top panel) and trigonal (bottom panel) distortions projected on the $[\varepsilon_a, \varepsilon_{c/d}]$ plane.

scalars ε_a , $\varepsilon_{c/d}$. Since the lattice dynamics calculations are one order of magnitude more time consuming than the total energy calculations, we used a coarser grid (see Fig. 10 for details on the grid).

The eigenvalues of each dynamical matrix are Fourier-interpolated in order to obtain smooth and continuous phonon dispersions. The zero-point energy and the thermal contributions are calculated by numerical integration over $21 \times 21 \times 21$ points in reciprocal space. This is essential to obtain numerically accurate values of the vibrational contribution.

Like for the case of the static contribution, we determined the best polynomial necessary to fit our data over the entire temperature range from 0 to 1000 K. Similarly, we used the adjusted R^2 and the AAE as indicators of the quality of the fit. We also checked *a posteriori* the convergence of the elastic constant curves obtained by fitting to different polynomial degrees. In the tetragonal case, a quadratic bivariate polynomial (i.e. 6 parameters) is sufficient to accurately reproduce the distribution of data points. On the other hand, for the trigonal deformation, a 4th order bivariate polynomial (i.e. 16 parameters) is needed.

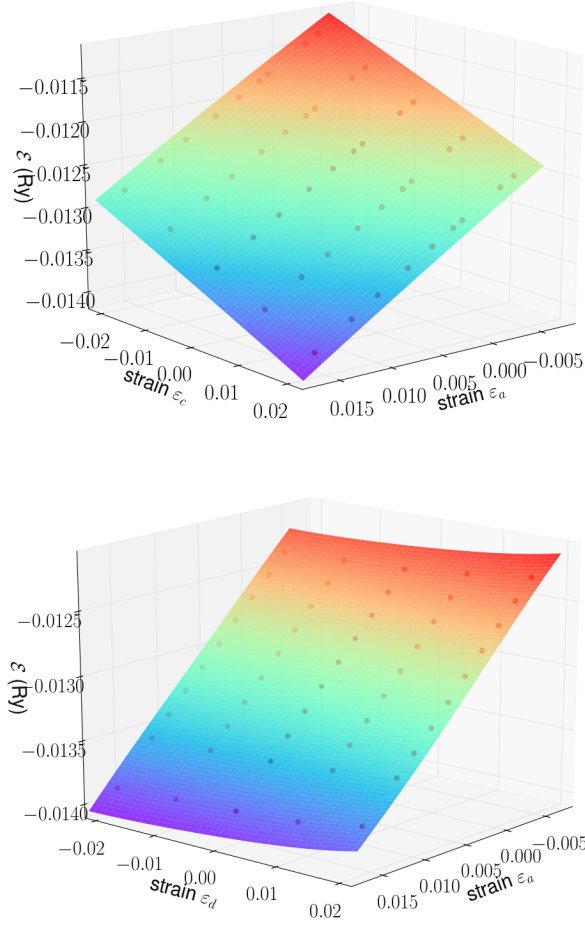


FIG. 10. Vibrational quasi-harmonic contribution to the Helmholtz free energy at $T = 750$ K in the $[\varepsilon_a, \varepsilon_c]$ space (top panel), $[\varepsilon_a, \varepsilon_d]$ space (bottom panel). A 2nd and a 4th order bivariate polynomial are respectively used to fit the tetragonal and trigonal data sets.

Our choice of polynomial is dictated by the need to minimize the AAE, maximize R^2 and minimize the confidence interval as a function of temperature (see Supplemental Material⁶⁷ for the stability of the results against other polynomials). As an illustration, we report the vibrational energy landscape at 750 K for the tetragonal and for the trigonal distortions (Fig. 10).

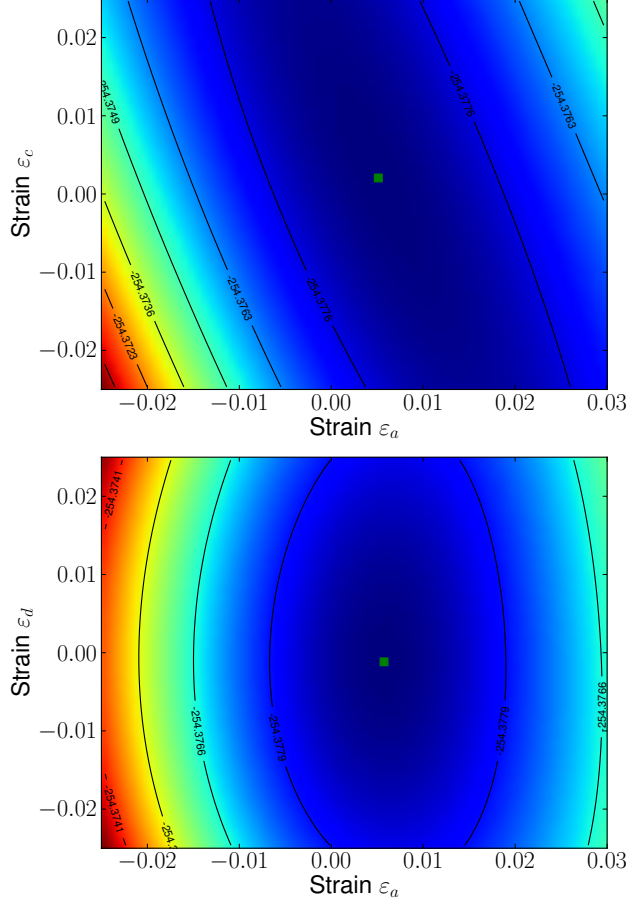


FIG. 11. Free energy landscape of the tetragonal (top panel) and trigonal (bottom panel) deformations projected on the $[\varepsilon_a, \varepsilon_d]$ and $[\varepsilon_a, \varepsilon_c]$ plane respectively at 500 K. The green squares represent the minima of the energy landscapes.

3. Evaluation of the elastic constants

Next, we sum the static and vibrational energy landscapes obtained in the previous sections and compute the Helmholtz free energy. An example of the resulting landscape at 500 K is displayed in Fig. 11. The second derivative with respect to strain can be evaluated analytically at the minimum of the free energy as a function of temperature.

Then, in order to understand if the discrepancy between the experimental and calculated elastic constants could be ascribed to the fitting procedure, we have calculated the confidence interval of C_{11} and C_{44} . To this end, we have computed the covariance matrix of each best-fit

contribution to the free energy, defined as:

$$\text{cov}(P) = \sigma_r^2 (J^T J)^{-1}, \quad (10)$$

where P is the set of polynomial coefficients, σ_r^2 is the squared residual and J is the Jacobian matrix which is provided in output by the least squares routine. The global variance of each best fit polynomial is then obtained by considering both the diagonal and the off-diagonal elements of the covariance matrix $\text{cov}(P)$. Finally, we used error-propagation theory to obtain the confidence interval of the elastic constants.

The calculated C_{11} and C_{44} elastic constants of BCC α -iron both decrease by increasing temperature, as shown in Fig. 12. Our results are in reasonable accordance with those reported in Ref. 68 (the exception is C_{44} that in our case is fairly underestimated) where, however, a direct detailed comparison with experimental thermal softening is clearly more difficult. In Tab. III, we report their zero temperature values with and without zero-point energy (ZPE) contributions, thus comparing these to experimental values. Also, for sake of completeness, we report in Tab. IV the $C_{12} = \frac{3B-C_{11}}{2}$, $C' = \frac{1}{2}(C_{11} - C_{12}) = \frac{3}{4}(C_{11} - B)$ and anisotropy ratio C_{44}/C' obtained from standard theory of elasticity and our calculated B , C_{11} and C_{44} (see Fig. 13 for the temperature dependence of the C'). The inclusion of ZPE results in a small decrease of the elastic constants and bulk modulus. The confidence interval at zero temperature is of the order of 0.1 GPa and cannot account for the difference with respect to experiments, so we will discuss other possible source of this discrepancy in the next section.

T (K)	a (Å)	B (GPa)	C_{11} (GPa)	C_{44} (GPa)
0 (no ZPE)	2.834	199.8±0.1	296.7±0.3	104.7±0.1
0 (ZPE)	2.839	194.6±0.3	287.9±0.4	102.2±0.5
0 (Expt.) ^{36,50}	2.856	170.3±1	239.5±1	120.7±0.1

TABLE III. Calculated 0 K elastic constants for iron with and without zero-point energy contributions. Results are compared to experimental data extrapolated to 0 K.

T (K)	C_{12} (GPa)	C' (GPa)	C_{44}/C'
0 (no ZPE)	151.4 ± 0.2	72.7 ± 0.3	1.44
0 (ZPE)	148.01 ± 0.5	70.0 ± 0.4	1.46
0 (Expt.) ⁵⁰	135.7	51.9	2.32

TABLE IV. C_{12} and C' elastic constants, and C_{44}/C' anisotropy ratio, derived from Tab. III with and without zero-point energy. Results are compared to experimental data extrapolated at 0 K. Errors are obtained according to propagation of uncertainties.

C. Discussion

The temperature dependence of the bulk modulus and of the elastic constants display an overall good agreement with the available experimental data, showing how lattice vibrations alone provide a robust description of the thermoelastic properties of the material, especially below the Debye temperature Θ_D . The agreement is still valid above Θ_D for the C_{44} , that shows a near-linear behavior generally expected for metallic systems according to the semiempirical Varshni equation⁶⁹. On the other hand, approaching the Curie temperature (1043 K) from below, the results are not able to reproduce the anomalous non-linear softening which is observed in experimental B and C_{11} .

According to previous work, e.g. based on a tight-binding approximation coupled to a single-site spin-fluctuation theory of band magnetism⁶³, effective spin-lattice couples models⁶⁴ as well as experiments^{25,26}, the origin of these anomalies is inherently related to magnetic fluctuations and, ultimately, to their influence on the free energy landscape (via modulation of the exchange couplings, configurational disorder and magnon-phonon interaction). In support of this conclusion, previous ab-initio papers^{11,23} suggest that the electronic entropy and phonon-phonon anharmonic effects beyond the quasiharmonic approximation play a minor role in determining the thermodynamics of the system below T_C . Given the strong indications of the pivotal role of magnetism in the description of thermoelastic properties of α -iron close to the Curie temperature, further ab-initio calculations taking into account magnetic disorder would be of paramount interest (see for instance Ref. 24).

Focusing instead on the 0 K structural and elastic properties, we now discuss the possible origin of the mismatch between the calculated and experimental values. As we showed earlier, our calculated points are numerically accurate, and the errors associated with the

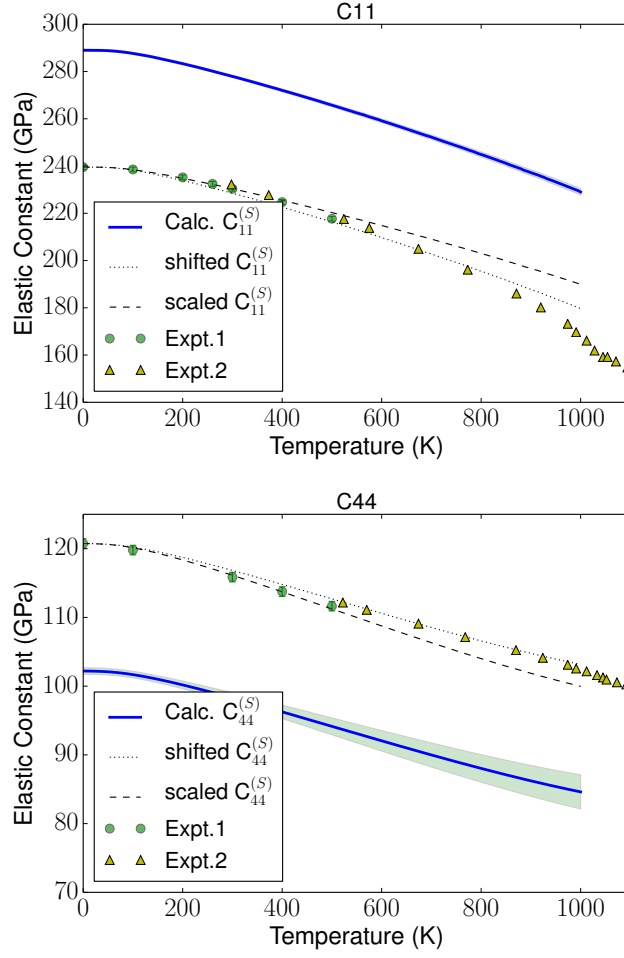


FIG. 12. Top panel: calculated adiabatic C_{11} elastic constant (blue solid line). Bottom panel: calculated adiabatic C_{44} (blue solid line). Two sets of experimental data are reported on each plot – Expt.1 (green circles) from Ref. 50 and Expt.2 (yellow triangles) from Ref. 26. The calculated interval of confidence is displayed as a shaded area. As a guide to the eye, we also plot the elastic constants rigidly shifted (dotted line) and scaled (dashed line) to match the experimental values at zero temperature.

fit are fairly small. As a consequence, the origin of the discrepancy can be ascribed (i) to the presence of magnetic domain walls, (ii) to the pseudopotential approximation, (iii) to the approximate XC functional.

First, we inspected the possible effects on the equilibrium volume at 0 K due to the presence of magnetic domain walls. We focus our attention to the collinear domain wall case, thus mimicking a magnetic distribution of domains in iron as two 8-atoms-thick ferromag-

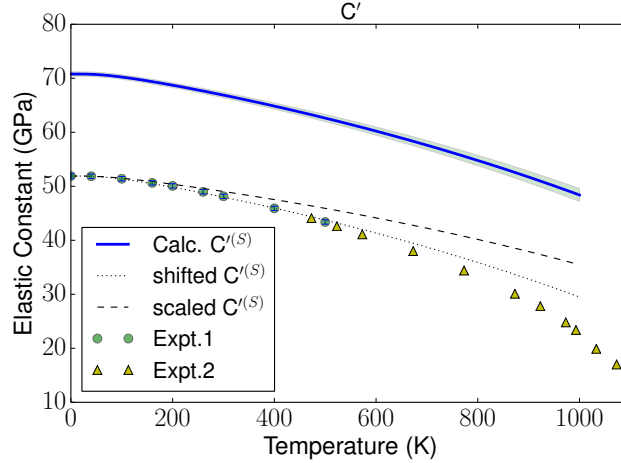


FIG. 13. Thermal behavior of the C' elastic constant calculated as a linear combination of $B(T)$ and $C_{11}(T)$ (blue continuous line). Two sets of experimental data are reported – Expt.1 (green circles) from Ref. 50 and Expt.2 (yellow triangles) from Ref. 26. The calculated interval of confidence is displayed as a shaded area. As a guide to the eye, we also plot the elastic constants rigidly shifted (dotted line) and scaled (dashed line) to match the experimental values at zero temperature.

netic strips with antiparallel magnetic moments repeated in the z direction through periodic boundary conditions. The effect due the interfaces is to increase the lattice parameter of about 0.7% and to decrease the bulk modulus of about 9%. Since the density of domain walls in real materials is expected to be an order of magnitude lower, the effect on the lattice parameter should be rescaled accordingly, thus suggesting that domain walls affects only marginally the value of the equilibrium lattice parameter at 0 K.

Next, we have observed that, for a given XC functional, details of the pseudopotential can have a large impact on the calculated quantities. For instance, in the case of PBE, the bulk modulus at 0 K ranges from 165 to 201 GPa if we consider pseudopotentials generated by different authors: ultrasoft or PAW, with 8 or 16 electrons or, even using the same electronic configuration but different version of *pslibrary*⁷⁰ (see Figs. 1, 2).

As discussed in Sec. III, the pseudopotential used in this work was chosen as being closest in its equation of state and its magnetization as a function of volume to all-electron FLAPW calculations^{45 71}. As a result, the discrepancy at 0 K with respect to experiments found in this work and in all-electron calculations seems ascribable mainly to the exchange-correlation functional used. For this reason, we explored the effect of the XC functional on the 0 K

properties, keeping the pseudopotential generation scheme and parameters unchanged. We performed test calculations with the WC⁴¹ and PBEsol⁴² functionals, and found that the disagreement with the experimental data is increased (see Figs. 1, 2).

Eventually, we observe that the QHA thermal contribution to the energy landscape is almost linear (see Fig. 10) and does not contribute too much to the total curvature in the energy landscape. Moreover, its change in second derivative along with temperature is even smaller, and only marginally contributes to the temperature dependence of the total curvature of the energy landscape (its main effect is to shift the minimum of the free energy as a function of temperature). Therefore, we conclude first that the mismatch with experiments at finite temperature is dominated by the 0 K static contribution discussed above. Second, that the temperature dependence of the elastic constants is driven, in first approximation, by the curvature of the 0 K energy landscape at the equilibrium expanded volumes. Our finding suggests that one could try and employ more computationally expensive methods (such as DFT+U+J^{40,72}, hybrid functionals⁷³, RPA^{74,75} or DMFT^{76,77}) to explore possible improvements in the description of the 0 K mechanical properties of α -iron, while thermal properties can be determined using lattice dynamics calculations performed with standard semi-local GGA functionals.

V. CONCLUSIONS

We have calculated the isothermal and adiabatic elastic constants of α -iron as a function of temperature from first-principles, using pseudopotential total energy calculations based on DFT and lattice dynamics calculations based on DFPT, out of which we calculate free energies in the quasiharmonic approximation and finite-temperature elastic constants from small strain deformations. Great care has been put in the verification of the pseudopotentials, and the validation of the results against experiments. Common semi-local DFT functionals such as PBE reproduce only fairly elastic constants at zero temperature; on the other hand, their thermal behavior, originating from the changes in phonon dispersions upon crystal expansion, is very well described by the same functionals and in the quasiharmonic approximation, with a softening of the elastic constants and bulk modulus that is in excellent agreement with experiments up to Θ_D and above. This work was supported by a grant from the Swiss National Supercomputing Centre (CSCS) under project ID *ch3*. We

would like to acknowledge P. Pavone and C. Draxl for their kind support in calculating and providing all-electron data with the **exciting** code as well as S. Cottenier for providing all-electron data obtained with the WIEN2K code that were used for comparison with available pseudopotentials. We also acknowledge partial support from the FP7-MINTWELD project.

-
- ¹ M. J. Alfè, D. Gillan and G. D. Price, *Nature* **401**, 462 (1999).
 - ² W. Kohn and L. J. Sham, *Phys. Rev.* **140**, A1133 (1965).
 - ³ S. Baroni, S. de Gironcoli, A. Dal Corso, and P. Giannozzi, *Rev. Mod. Phys.* **73**, 515 (2001).
 - ⁴ S. Baroni, P. Giannozzi, and E. Isaev, *Rev. Mineral. Geochem.* **71**, 39 (2010).
 - ⁵ P. Pavone, S. Baroni, and S. de Gironcoli, *Phys. Rev. B* **57**, 10421 (1998).
 - ⁶ A. A. Quong and A. Y. Liu, *Phys. Rev. B* **56**, 7767 (1997).
 - ⁷ N. Mounet and N. Marzari, *Phys. Rev. B* **71**, 205214 (2005).
 - ⁸ A. J. Hatt, B. C. Melot, and S. Narasimhan, *Phys. Rev. B* **82**, 134418 (2010).
 - ⁹ A. Debernardi, M. Alouani, and H. Dreyssé, *Phys. Rev. B* **63**, 064305 (2001).
 - ¹⁰ S. Narasimhan and S. de Gironcoli, *Phys. Rev. B* **65**, 064302 (2002).
 - ¹¹ X. Sha and R. E. Cohen, *Phys. Rev. B* **73**, 104303 (2006).
 - ¹² R. Golesorkhtabar, P. Pavone, J. Spitaler, P. Puschnig, and C. Draxl, *Computer Physics Communications* **184**, 18611873 (2013).
 - ¹³ M. J. Mehl, J. E. Osburn, D. A. Papaconstantopoulos, and B. M. Klein, *Phys. Rev. B* **41**, 10311 (1990).
 - ¹⁴ S. Baroni, P. Giannozzi, and A. Testa, *Phys. Rev. Lett.* **59**, 2662 (1987).
 - ¹⁵ X. Wu, D. Vanderbilt, and D. R. Hamann, *Phys. Rev. B* **72**, 035105 (2005).
 - ¹⁶ D. R. Hamann, X. Wu, K. M. Rabe, and D. Vanderbilt, *Phys. Rev. B* **71**, 035117 (2005).
 - ¹⁷ Z. Wu and R. M. Wentzcovitch, *Phys. Rev. B* **83**, 184115 (2011).
 - ¹⁸ R. M. Wentzcovitch, B. B. Karki, M. Cococcioni, and S. de Gironcoli, *Phys. Rev. Lett.* **92**, 018501 (2004).
 - ¹⁹ Y. Wang, J. J. Wang, H. Zhang, V. R. Manga, S. L. Shang, L.-Q. Chen, and Z.-K. Liu, *Journal of Physics: Condensed Matter* **22**, 225404 (2010).
 - ²⁰ A. R. Oganov, J. P. Brodholt, and G. D. Price, *Nature* **411**, 934 (2001).
 - ²¹ D. C. Wallace, *Thermodynamics of crystals*, edited by D. publications Inc. (1972).

- ²² M. J. Verstraete, *Journal of Physics: Condensed Matter* **25**, 136001 (2013).
- ²³ F. Körmann, A. Dick, B. Grabowski, B. Hallstedt, T. Hickel, and J. Neugebauer, *Phys. Rev. B* **78**, 033102 (2008).
- ²⁴ F. Körmann, A. Dick, B. Grabowski, T. Hickel, and J. Neugebauer, *Phys. Rev. B* **85**, 125104 (2012).
- ²⁵ L. Mauger, M. S. Lucas, J. A. Muñoz, S. J. Tracy, M. Kresch, Y. Xiao, P. Chow, and B. Fultz, *ArXiv e-prints* (2014), arXiv:1404.4998 [cond-mat.mtrl-sci].
- ²⁶ D. J. Dever, *J. Appl. Phys.* **43**, 3293 (1972).
- ²⁷ P. Giannozzi, S. Baroni, N. Bonini, M. Calandra, R. Car, C. Cavazzoni, D. Ceresoli, G. L. Chiarotti, M. Cococcioni, I. Dabo, A. Dal Corso, S. de Gironcoli, S. Fabris, G. Fratesi, R. Gebauer, U. Gerstmann, C. Gougoussis, A. Kokalj, M. Lazzeri, L. Martin-Samos, N. Marzari, F. Mauri, R. Mazzarello, S. Paolini, A. Pasquarello, L. Paulatto, C. Sbraccia, S. Scandolo, G. Sclauzero, A. P. Seitsonen, A. Smogunov, P. Umari, and R. M. Wentzcovitch, *Journal of Physics: Condensed Matter* **21**, 395502 (19pp) (2009).
- ²⁸ J. P. Perdew, K. Burke, and M. Ernzerhof, *Phys. Rev. Lett.* **77**, 3865 (1996).
- ²⁹ D. Vanderbilt, *Phys. Rev. B* **41**, 7892 (1990).
- ³⁰ For iron, this is identical to 0.2.1.
- ³¹ This pseudopotential is uniquely labeled as `Fe.pbe-spn-rrkjus-ps1.0.2.1.UPF`.
- ³² N. Marzari, D. Vanderbilt, A. De Vita, and M. C. Payne, *Phys. Rev. Lett.* **82**, 3296 (1999).
- ³³ <http://www.qe-forge.org/gf/project/pslibrary>.
- ³⁴ <http://www.physics.rutgers.edu/gbrv/>.
- ³⁵ G. Kresse and J. Furthmüller, *Phys. Rev. B* **54**, 11169 (1996).
- ³⁶ Z. S. Basinski, W. Hume-Rothery, and A. L. Sutton, *Proceedings of the Royal Society of London. Series A. Mathematical and Physical Sciences* **229**, 459 (1955).
- ³⁷ V. I. Anisimov and O. Gunnarsson, *Phys. Rev. B* **43**, 7570 (1991).
- ³⁸ V. I. Anisimov, J. Zaanen, and O. K. Andersen, *Phys. Rev. B* **44**, 943 (1991).
- ³⁹ V. I. Anisimov, F. Aryasetiawan, and A. I. Lichtenstein, *Journal of Physics: Condensed Matter* **9**, 767 (1997).
- ⁴⁰ B. Himmetoglu, A. Floris, S. de Gironcoli, and M. Cococcioni, *International Journal of Quantum Chemistry* **114**, 14 (2014).
- ⁴¹ Z. Wu and R. E. Cohen, *Phys. Rev. B* **73**, 235116 (2006).

- ⁴² J. P. Perdew, A. Ruzsinszky, G. I. Csonka, O. A. Vydrov, G. E. Scuseria, L. A. Constantin, X. Zhou, and K. Burke, Phys. Rev. Lett. **100**, 136406 (2008).
- ⁴³ P. Blaha, K. Schwarz, P. Sorantin, and S. Trickey, Computer Physics Communications **59**, 399 (1990).
- ⁴⁴ A. Gulans, S. Kontur, C. Meisenbichler, D. Nabok, P. Pavone, S. Rigamonti, S. Sagmeister, U. Werner, and C. Draxl, Journal of Physics: Condensed Matter **26**, 363202 (2014).
- ⁴⁵ K. Lejaeghere, V. Van Speybroeck, G. Van Oost, and S. Cottenier, Critical Reviews in Solid State and Materials Sciences **39**, 1 (2014), <http://dx.doi.org/10.1080/10408436.2013.772503>.
- ⁴⁶ P. Pavone private communication. **exciting** code (*'boron'* version), PBE functional, rmt=2.00 Bohr, rgkmax=9.0 Bohr, $24 \times 24 \times 24$ k -mesh, Gaussian smearing, smearing width=0.002 Ha, nempty=15, gmaxvr=12 (2014).
- ⁴⁷ <https://molmod.ugent.be/deltacodesdft>.
- ⁴⁸ H. Ebert, Zeitschrift für Physik **47**, 712 (1928).
- ⁴⁹ F. C. Nix and D. MacNair, Phys. Rev. **60**, 597 (1941).
- ⁵⁰ J. J. Adams, D. S. Agosta, R. Leisure, and H. Ledbetter, Journal of Applied Physics **100**, 113530 (2006).
- ⁵¹ S. Cottenier private communication. WIEN2K code (13.1 version), PBE functional, rmt=1.8, rkmax=10.0, $36 \times 36 \times 36$ k -mesh, Fermi-Dirac smearing, smearing width=0.001 Ry (2014).
- ⁵² H. L. Zhang, S. Lu, M. P. J. Punkkinen, Q.-M. Hu, B. Johansson, and L. Vitos, Phys. Rev. B **82**, 132409 (2010).
- ⁵³ For the GBRV and rrkjus-1.0.0 pseudopotentials reported in Fig. 3 instead, the anomaly starts around +4/5% of their equilibrium volume and the magnetization is systematically overestimated if compared to all-electron data.
- ⁵⁴ F. Birch, Phys. Rev. **71**, 809 (1947).
- ⁵⁵ See EPAPS Document No.[].
- ⁵⁶ A. Dal Corso and S. de Gironcoli, Phys. Rev. B **62**, 273 (2000).
- ⁵⁷ S. Klotz and M. Braden, Phys. Rev. Lett. **85**, 3209 (2000).
- ⁵⁸ B. Brockhouse, H. Abou-Helal, and E. Hallman, Solid State Communications **5**, 211 (1967).
- ⁵⁹ N. Ridley and H. Stuart, J. Phys. D: Appl. Phys. **1**, 1291 (1968).
- ⁶⁰ I. S. Grigoriev and E. Z. Melikhov, *Handbook of Physical Quantities* (CRC Press, Boca Raton, 1997).

- ⁶¹ P. D. Desai, Journal of Physical and Chemical Reference Data **15**, 967 (1986).
- ⁶² D. C. Wallace, P. H. Sidles, and G. C. Danielson, Journal of Applied Physics **31**, 168 (1960).
- ⁶³ H. Hasegawa, M. W. Finnis, and D. G. Pettifor, J. Phys. F: Met. Phys. **15**, 19 (1985).
- ⁶⁴ J. Yin, M. Eisenbach, D. M. Nicholson, and A. Rusanu, Phys. Rev. B **86**, 214423 (2012).
- ⁶⁵ C. Kittel, *Introduction to Solid State Physics*, 6th ed. (John Wiley & Sons, Inc., New York, 1986).
- ⁶⁶ We used the least squares method routine `scipy.optimize.leastsq` which is a wrapper around the Fortran routine *lmdif* of MINPACK⁷⁸.
- ⁶⁷ See EPAPS Document No.[].
- ⁶⁸ X. Sha and R. E. Cohen, Phys. Rev. B **74**, 214111 (2006).
- ⁶⁹ Y. P. Varshni, Phys. Rev. B **2**, 3952 (1970).
- ⁷⁰ <http://www.qe-forge.org/gf/project/pslibrary>.
- ⁷¹ P. Pavone and S. Cottenier, private communications as reported above.
- ⁷² B. Himmetoglu, R. M. Wentzcovitch, and M. Cococcioni, Phys. Rev. B **84**, 115108 (2011).
- ⁷³ J. Paier, M. Marsman, K. Hummer, G. Kresse, I. C. Gerber, and J. G. ngyn, The Journal of Chemical Physics **124**, 154709 (2006).
- ⁷⁴ H.-V. Nguyen and S. de Gironcoli, Phys. Rev. B **79**, 205114 (2009).
- ⁷⁵ L. Schimka, R. Gaudoin, J. c. v. Klimeš, M. Marsman, and G. Kresse, Phys. Rev. B **87**, 214102 (2013).
- ⁷⁶ G. Kotliar, S. Y. Savrasov, K. Haule, V. S. Oudovenko, O. Parcollet, and C. A. Marianetti, Rev. Mod. Phys. **78**, 865 (2006).
- ⁷⁷ L. V. Pourovskii, J. Mravlje, M. Ferrero, O. Parcollet, and I. A. Abrikosov, Phys. Rev. B **90**, 155120 (2014).
- ⁷⁸ J. J. Moré, B. S. Garbow, and K. E. Hillstom, *User Guide for MINPACK-1*, Tech. Rep. ANL-80-74 (Argonne National Laboratory, Argonne, IL, USA, 1980).